Requirements for the detectors and read-out of ATHENA X-IFU

R. den Hartog[*1], D. Barret[2], L. Gottardi[1], J.-W. den Herder[1], B. Jackson[3], P. de Korte[1], J. van der Kuur[1], B-J van Leeuwen[1], D. van Loon[1], A. Nieuwenhuizen[1], L. Ravera[2]

[1] SRON Netherlands Institute for Space Research, Sorbonnelaan 2, 3584CA Utrecht, The Netherlands
[2] CNRS, IRAP Institut de Recherche en Astrophysique et Planétologie, 9 Avenue du Colonel Roche, BP 44346, 31028 Toulouse Cedex 4, France
[3] SRON Netherlands Institute for Space Research, Landleven 12, 9700 AV Groningen, The Netherlands

ABSTRACT

The detector system of the X-Ray Integral Field Unit (X-IFU), one of the two ATHENA focal plane instruments will be an ambitious step forward in the field of astronomical X-ray detection. We describe its baseline configuration, consisting of 3840 Transition Edge Sensors (TES) microcalorimeters with an energy resolution of 2.5 eV FWHM, spanning a 5 arcminute field-of-view and allowing an imaging resolution of 5 arcsec. The detectors are read out in 96 channels of 40 pixels each, using frequency domain multiplexing (FDM). Each channel contains a dual-stage SQUID pre-amplifier and a low-noise amplifier (LNA). In order to enhance the dynamic range of the SQUIDs a specific technique, baseband feedback (BBFB), is applied. The generation of the carrier and feedback signals, and the signal processing are done in the digital domain. We review the requirements for the main elements of this system, needed to ensure the high performance of the detector system. From the resolution requirements for the detectors follows a budget for contributions to the energy resolution on top of the intrinsic detector resolution. This budget forms the basis for the assessment of the dynamic range requirements for the SQUID and the LNA and the DACs and the ADC. Requirements are also derived for the levels of crosstalk and non-linearity in the readout chain.

Keywords: Microcalorimeters, Transition Edge Sensors, Frequency Domain Multiplexing, Athena, X-IFU

1. INTRODUCTION

The Athena mission concept [1][2] has been proposed to the European Space Agency in response to their call for missions to address the Cosmic Vision theme *The Hot and Energetic Universe*, chosen last year for the L2 launch slot in 2028. The mission concept addresses 8 science goals, plus 5 optional science goals, which focus on answering the two fundamental astrophysical questions of the theme:

- How does ordinary matter assemble into the large scale structure that we observe today?
- How do black holes grow and shape the Universe?

The X-IFU instrument [3], which is being developed for Athena by an IRAP-led consortium, is the answer to the request for high-resolution imaging spectroscopy, which is a crucial tool for addressing these science questions. For this instrument, a list of top-level requirements have been derived based on the science cases, which is further broken down in more detailed requirements in this paper. Compared to its predecessor, the XMS instrument proposed for the IXO mission [4], the array design, the detectors and the readout system on X-IFU will be different, which motivates a reassessment of the requirements. As the development of the detectors is ongoing [5], only a tentative baseline design can be established at the moment. The goal of this tentative baseline is to provide guidelines and derived requirements for design studies of the detectors, cooler and the focal-plane array which will soon commence, rather than to provide a

[*] r.h.den.hartog@sron.nl; phone +31-88-777-5678

final design for the instrument. The baseline is chosen to be conservative with regards to technology development and cooler requirements, in order to create some design margin in areas where the performance limits are less well known, such as the detectors. In this paper, we will focus mainly on the dynamic range requirements for the readout chain, ensuring that the updated set of instrument requirements does not lead to unfeasible demands on the readout hardware.

2. ATHENA X-IFU DETECTOR SYSTEM REQUIREMENTS

We start with recalling the top-level instrument requirements, as defined in Ref. [3], derived from a set of 8 science goals. Only the requirements pertinent to the X-IFU instrument are listed in Table 1.

Parameter	Requirement
Energy range	0.2 - 12 keV
Energy resolution: E < 7 keV	2.5 eV FWHM
Energy resolution: E > 7 keV	$E/\Delta E = 2800$
Field of view	≥ 5 arcmin Ø
Size of pixels	≤ 5 x 5 arcsec^2
Quantum efficiency[a] @ 1 keV	> 60%
Quantum efficiency[a] @ 7 keV	> 70%
Energy (gain) stability	0.4 eV
Countrate capability: faint point source	1 mCrab (with > 80% high resolution events)
Countrate capability: strong point source	10 mCrab (with > 30% high resolution events)
Time resolution	10 μs
Non X-ray background[b]	< 5 10^{-3} counts / s / cm^2 / keV

[a] QE includes here absorber stopping power, pixel filling factor and optical blocking filters
[b] After application of the Cryogenic Anti-coincidence detection

Table 1. Requirements for the key performance parameters of the Athena X-ray Integral Field Unit.

2.1 Detector array

One of the most important differences between the current X-IFU baseline array and the previous IXO array is that for X-IFU a uniform array has been chosen, as required by high-resolution spectroscopy of extended objects, such as the hot gas in galaxy clusters. From the requirements on the field of view and the angular size of the individual pixels, the resulting detector array will have on the order of 3600 pixels.

In Table 2, a trade-off is made between three basic detector array shapes – circular, hexagonal and square – where we take into account the heatload on the cold stages of the cooler. Note that the hexagonal shape does not have exact 120° angles as it is based on square pixels. One basic assumption here is that up to 40 pixels can be multiplexed in one channel of 4 MHz wide. This number is an extrapolation from analyses made during the IXO system assessment [6], and assuming the information bandwidth of the pixels can be sufficiently reduced. The analysis below shows that this assumption is consistent with dynamic range and crosstalk requirements. An upper limit of ~100 channels has been placed as mechanically and thermally feasible, hence two possible detector absorber sizes are considered. The trade-off also includes the length of the snout of the magnetic shield, which drives up the mass of the shield and thus contributes to the mass at 50 mK, but will also drive up the size and mass of the cooler, via the required cold working volume. Finally, we looked at the area on the sky that can be covered in 4 minimally overlapping exposures. From the table it is clear that the circular array is most economic and the square array already out of margin with respect to the number of channels.

In line with the philosophy of keeping design margin, we have taken the hexagonal array shape as a baseline for the mechanical design of the focal plane assembly [7], but use the circular configuration of 240 μm pixels for the detector array baseline. We allow for a 15 μm spacing (which is the minimum lithographically feasible for thick Bi absorber layers), and added 1 channel margin to the 95 required, in case we want to have one test or reference pixel per channel. Thus the baseline readout system contains the capacity for 3840 pixels, divided over 96 channel, with 40 pixels each.

Criteria	square	Hexagon	circular
	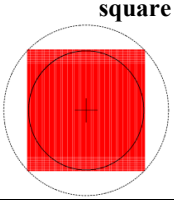	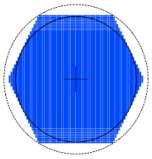	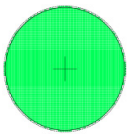
Number of 240 μm pixels required to fully cover a 5' FoV	4761	4164	3768
+ number of channels with 40 pixels / channel multiplexing	120	105	95
Number of 250 μm pixels required to fully cover a 5' FoV	4356	3804	3496
+ number of channels with 40 pixels / channel multiplexing	109	96	88
Relative shield aperture diameter = relative snout length	1.41	1.17	1.0
Relative shield mass increase	8%	3%	0%
Minimum diameter of circular field with 4 FoVs stitched together and minimum but finite overlap	9.4'	7.5'	7.1'
Maximum dimension in field with 4 fields stitched together	13.2'	14.8'	10.0'
Minimum amount of overlap (% of total observed area)	1.6%	1.0%	18%

Table 2. Trade-off of array shape. The illustrations show the difference between the sampled FoV (inner circle) and the (projected) required opening angle of the magnetic shield (outer circle).

2.2 Baseline detector

Table 3 summarizes the main physical properties of a baseline TES-based microcalorimeter, compatible with the requirements in Table 1. These requirements needs to be broken down into an intrinsic detector performance and additional factors due to read-out and environment (see Section 3.3, below).

Parameter	Requirement	Comments
Intrinsic energy resolution ΔE_{int}	2.1 eV	Allows for contributions from read-out and environment
Saturating energy E_{lin}	> 7 keV	Avoids complex filtering schemes for energies where resolution is important.
Countrate capability	> 40 cps	With < 20% events suffering from resolution-degrading pile-up
Sensor absorber pitch	255 μm	Driven by pixel count and field-of-view requirement
Filling factor	> 85%	Defined as working pixel area / array area. This requirement includes area lost to dead pixels.
Absorber stopping power	> 90%	Requires the equivalent of ~5 μm Bi at 6 keV and ~7 μm Bi at 7 keV

Table 3. Required characteristics of the baseline X-IFU microcalorimeter.

The driving requirement is the energy resolution. Table 1 provides a requirement on the detector system performance, which translates into a requirement on the intrinsic detector resolution ΔE_{int} of 2.1 eV FWHM for 7 keV photons (see Section 3.3), where the relation for ΔE_{int} is [8]:

$$\Delta E_{int} = \sqrt{4\ln 4}\sqrt{4kT_C E_{lin}\gamma}, \text{ with } E_{lin} = \eta\frac{CT_C}{\alpha} \text{ and } \gamma = \sqrt{nF(1+2\beta)(1+M^2)}\,.$$

Here, the factor $[4\ln 4]^{1/2}$ converts a one-sigma width into a FWHM, T_C is the transition temperature of the TES, E_{lin} is the maximum energy of the linear regime of the detector and the γ parameter quantifies non-linear corrections to the (linear) Johnson noise, of which the first-order correction $(1+2\beta)$ is fully understood [9], while the M parameter has a more empirical character [10][11]. Furthermore, η is a proportionality parameter (determined experimentally to be about 0.8) [12], C is the total TES heat capacity, α is the dimensionless temperature sensitivity of the TES, β is the dimensionless current sensitivity of the TES, n is the power of the relation that describes the thermal link to the bath, and F quantifies the temperature gradient across the link, and is usually taken to be 0.5. Where T_C and E_{lin} can be controlled by design, the γ parameter turns out to much more difficult to control.

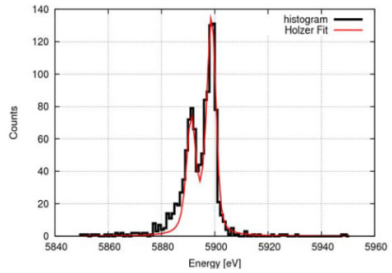

ΔE_{meas}(5.9 keV) = 4.0 eV
$\Delta E_{baseline}$ = 4.0 eV

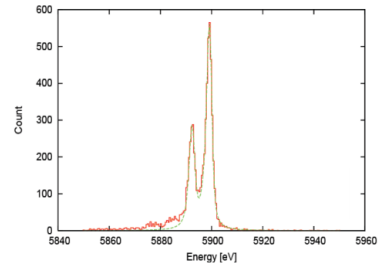

ΔE_{meas}(5.9 keV) = 2.5 eV
$\Delta E_{baseline}$ = 2.4 eV

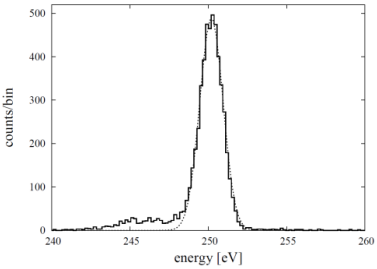

ΔE_{meas}(250 eV) = 1.7 eV at 500 cps countrate with 35% pile-up rejection
ΔE_{meas}(5.9 keV) = 2.5 eV

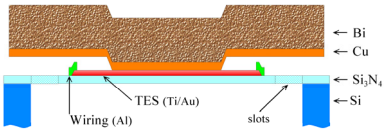

TES: TiAuTi: 20/55/5 nm
150 × 146 μm^2
Abs.: Cu/Bi: 0.15 / 3.0 μm
240 × 240 μm^2

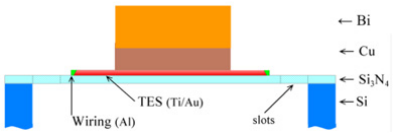

TES: TiAuTi: 50/20/5 nm
150 × 186 μm^2
Abs.: Cu/Bi: 1.0 / 2.64 μm
100 × 100 μm^2

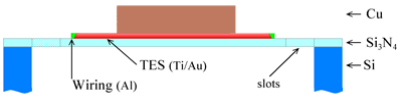

TES: TiAuTi: 20/50/5 nm
150 × 146 μm^2
Abs.: Cu: 1.0 μm
100 × 100 μm^2

Figure 1. Recapitulation of results obtained with SRON detectors up to 2010, when the development of TES-based detectors at SRON switched to bolometers. All measurements were made under DC conditions. From left to right: best result with a representative detector design [13], best result overall [13], and best result with high countrate [14].

Figure 1 summarizes the performance of previous designs by SRON [11][13][14], which demonstrated that under DC biasing conditions detectors with a small absorber could obtain the required energy resolution, at low energies even for countrates consistent with a ~12 mCrab point source. But these detectors also showed considerable non-linearity, and the attempt to extend the absorber to the required pixel size had a considerable impact on the energy resolution. Extrapolating from the measured properties of these detectors on the basis of the canonical first order detector model [15], it is not difficult to identify combinations of parameters that comply with the requirements in Table 3. The challenge lies in the physical realization of such a detector, e.g. a large absorber requires sufficiently fast heat diffusion to avoid response dependencies on photon absorption site, in combination with a heat capacity that does not drive the energy resolution beyond the limit, and an α parameter that does not push the M parameter too high. The NASA-GSFC group has demonstrated that such detectors are in principle feasible [16][17]. Their results also indicate that readout, in this case 2 channel times 8 pixel time-domain multiplexed (TDM), has a significant impact on the energy resolution, a fact that is confirmed by our own experience with a similar GSFC detector array under AC-biasing conditions and frequency-domain multiplexed (FDM) read-out [5][17][19].

The countrate specification follows from the requirement to observe point sources with a strength of at least 1 mCrab, which corresponds to a flux of 2.4 10^{-12} ergs / s / cm^2 = 2.4 fW / m^2 in the energy range 2 – 10 keV [20]. This translates into an 80 cps flux onto the X-IFU focal plane, when the geometry and transfer functions of the optics and the optical filters are taken into account [21]. Taking into account the 5" HEW of the optics point-spread function, the maximum countrate on a pixel is ~40 cps when the source is centered on the pixel, and ~20 cps when the source is located on a corner between four pixels. Assuming an event that allows around each pulse of $10\,\tau_{fall}$ before and $40\,\tau_{fall}$ after photon absorption, which reflects the need to sufficiently sample the low-frequency part of the pulse [22], and not taking into account possible algorithms for pile-up correction, an 80 cps countrate with 80% high-resolution (i.e pile-up free) events, is consistent with a pulse decay time τ_{fall} = 150 μs [3][4], so ~40 cps leaves a factor of 2 margin. With a similar τ_{fall} the requirement of 30% of pile-up free events for a 10 mCrab source can be met. When a 10 mCrab point source is centered on a pixel ~380 cps land on the central pixel, ~80 cps on its four nearest neighbours, and ~20 cps on its four diagonal neighbours. With τ_{fall} = 150 μs, this results in ~70% high-resolution events overall, cf. Fig. 9 in Ref. [3]. When the source is located on a corner, each of the four neighbours receive ~190 cps, which results in ~65% high-resolution

events. In both these cases, again a factor of 2 margin is present on the required >30% high-resolution events. To retain at least part of this margin we will work with τ_{fall} = 200 μs below.

3. ATHENA X-IFU READ-OUT REQUIREMENTS

3.1 Baseline read-out system

The detectors will be read out using Frequency Domain Multiplexing with Baseband Feedback [6][23]-[29]. FDM applies a set of sinusoidal AC carriers which bias the TES detectors in their set points and are amplitude modulated when the TES detectors sense a signal. The detectors are separated in frequency by placing them in series with LC filters of specific frequencies. It allows the read-out of multiple TES pixels (up to 40 in the baseline X-IFU design) in one amplifier channel which uses only one set of SQUID-based current sensors. This significantly reduces the wire count to the cold stage and hence the wiring complexity and heat-load on the cold stages of the instrument. In our application, BBFB cancels the summed signal in the SQUID and thus improves the dynamic range of the SQUID system.

Figure 2 shows a schematic of the baseline readout concept, highlighting the main elements of a single readout channel, but omitting auxiliary functionality like biasing of SQUIDs and LNA, SQUID offsets, housekeeping, command lines etc. The basic principles and main elements are discussed by Ravera et al. (2014) [29]. The frequency range of the carriers is limited to 1 to 5 MHz (with a possible option to extend to 6 MHz). The lower limit is determined by the physical size of the capacitors and inductors that form the LC filters. The inductance of the filter coils, 2 μH in the current baseline, is a trade-off between physical size of the LC filters and the required impedance environment of the TES, which determines electro-thermal feedback (ETF) stability and crosstalk. The upper limit of the frequency range is limited to 5-6 MHz by various factors, such as the maximum possible Q factor of the LC resonances, the minimum desirable resistance of the cable harness (hence part of the heat load on the 2K stage of the cooler), the maximum desirable power consumption of the digital electronics, and the bandwidth of the connection between the lower and upper stage SQUID. A final trade-off between minimum frequency spacing and maximum carrier frequency has therefore to be made.

The TES detectors are connected to the LC filters via flex cables which allows an out-of-plane configuration of the focal-plane assembly [7]. The connection between the chip with the detector array and the flex cables is foreseen to be in the form of a transformer coupling, which allows to rework the assembly, but also permits additional tuning of the TES impedance environment. A two-stage SQUID assembly, consisting of a low-power single SQUID at the 50 mK level and a high-power SQUID array at the 2K stage, provides the pre-amplification of the summed signals to a level sufficiently above EMI and EMC noise sources as to not reduce the dynamic range of the readout chain.

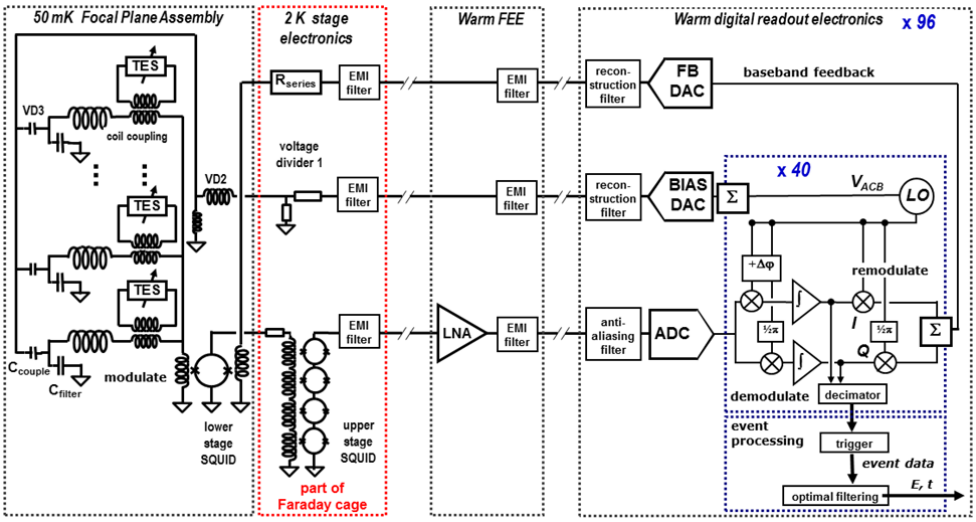

Figure 2. Simplified schematic of a single readout channel in the present baseline for the X-IFU BBFB FDM read-out system.

3.2 Time constants

One requirement for stable voltage biasing in the ETF regime demands that the Thevenin equivalent resistance in series with the TES, R_{ESR}, which is in our circuits mainly due to imperfect LC filter capacitors, is smaller than the set-point resistance R_0 by a factor that in the limit of high ETF loopgain approaches 1 [15]. We take a factor of 10 as requirement (not a budget), so $R_{ESR} < 4$ mΩ or $Q > \omega L/R_{ESR} \cong 3000\,f$ [MHz]. In practice, our current lithographic processes quite consistently provide R_{ESR} of the order of 1.5 mΩ [30], which is low enough to ignore in the subsequent analysis. The pulse rise and decay time are given approximately by the electrical and effective thermal timescales, respectively [15]:

$$\tau_{rise} \cong \tau_{el} = \frac{L}{R_0(1+\beta)} \text{ and } \tau_{fall} \cong \tau_{eff} = \frac{1}{1+\mathscr{L}'}\tau_0, \text{ with } \tau_0 = \frac{C}{G},\ \mathscr{L} = \frac{P_0\alpha}{GT_0} \text{ and } \mathscr{L}' = \frac{\mathscr{L}}{1+\beta} \text{ the effective ETF loopgain.}$$

Another requirement for stable ETF operation is that the electrical inertia of the bias circuit is considerably smaller than the thermal inertia of the detector [15]. For AC biasing, the electrical filter time constant is related to the detector time constant by:

$$\tau_{el} \le \frac{3+\beta-2\sqrt{2+\beta}}{2(1+\beta)}\tau_{eff}$$

Where the extra factor 2 accounts for the fact that when the TES is operated under AC bias the effective inductance is twice that in the DC case [31]. This relation holds in the approximation of zero load impedance and is valid for $L \le 1$ μH when $\beta = 1$ and $R_0 = 40$ mΩ, which corresponds to ~$0.2R_N$. A larger value of L would be advantageous for two reasons: For $L = 2$ μH the LC filter surface area is minimal over the frequency range we are considering which allows the most compact focal-plane assembly [27], and a larger inductance also creates more margin for common impedance contributions to crosstalk, as will be discussed below. So we have two options: increasing the setpoint resistance (which implies changing R_N as well if we want to conserve detector dynamic range), or using the coil coupling between the (primary) TES circuit and the (secondary) LC filter circuit to transform the apparent setpoint resistance in the secondary circuit.

A related parameter which is important for the dimensioning of the readout system, is the information band of the detector, defined as the frequency where the electrical noise exceeds the phonon noise:

$$B = \frac{\sqrt{n}\mathscr{L}-1}{2\pi\tau_0} \approx \frac{\sqrt{n}}{2\pi\tau_{fall}}.$$

For the detectors in Fig. 1, $n \cong 3.5$, so a τ_{fall} of 200 μs would imply $B \cong 1.5$ kHz.

3.3 Preliminary noise budget

In a realistic instrument design we have to meet the energy resolution requirement in the presence of additional external factors that contribute to the energy resolution. The most challenging requirement is a FWHM energy resolution of 2.5 eV for 7 keV photons. Such an exercise has already been done for the XMS instrument during the IXO study, but since X-IFU will have different detectors, read-out and cooler systems, it is necessary to repeat this process. In order to create margin for the contributions from the readout and environment, we restrict the intrinsic energy resolution of the detector (the result of phonon, Johnson, and, possibly, excess noise) to 2.1 eV.

Among the factors in the read-out chain contributing to a degradation of the energy resolution are the SQUID and LNA noise, the noise from the DACs with which the carriers and the baseband feedback are generated, and the ADC, electrical crosstalk, finite event length, aliasing, drifts in bias and gain, higher order intermodulation spurs, etc… Among the factors in the environment contributing to the resolution degradation are EM interference, structure noise, interfering signals from low-energy photons and cosmic rays, thermal crosstalk, noise and drift on the bath temperature, noise and drifts in the magnetic fields, mechanical vibrations and microphonics. For both realms we can identify of the order of 10 different contributors, so for the moment we allow equal independent proportions for all the contributions of 0.25 eV, except for the carriers generated by DACs, for which we reserve 0.5 eV, for reasons which will be discussed below.

The root sum square of 22 independent contributions of 0.25 eV, two of 0.5 eV and 2.1 eV equals 2.5 eV. At this point, this budget can only be the starting point for a detailed trade-off exercise, fed with the results from development activities for detector, readout and cooler which will take shape the coming years.

3.4 Dynamic range requirements

Let A be a quantity in which the measured pulse is encoded in any step during the read-out process, which can be either current, voltage, flux or bits. Given a baseline white noise powerlevel a_n, in units of A/√Hz, V/√Hz, Φ_0/√Hz, and the peak value A_{peak} of an exponential pulse with a decay (fall) time τ, the resulting FWHM resolution is given by:

$$\frac{\Delta E}{E} = \frac{\sqrt{4\ln 4}}{\sqrt{\tau}} \frac{a_n}{A_{peak}} .$$

The term $\sqrt{4 \ln 4} \cong 2.3548$ converts rms into FWHM provided the distribution of energies is Gaussian.
The dynamic range (density) of channel A is defined as $DR = A_{pp} / a_n$, with the A_{pp} the peak-to-peak amplitude of the carrier, rather than the peak of the modulating pulse signal. In the conversion from A_{peak} to A_{pp} at least the following additional factors have to be taken into account:

- A factor 2 to convert a single-sided pulse peak into a peak-to-peak carrier amplitude,
- A factor √2 to account for the loss of dynamic range in the modulation - demodulation process [26]. This factor could be avoided by rotating the phase of each carrier in such a way that the I and Q signals after demodulation (see Fig. 2) align with the resistive and reactive part of the signal, respectively. Since all the information of the TES is in the resistive part of its signal, the noise in the Q channel can be avoided, together with reactive effects due to the weak-link behaviour of the TES [19][32][33]. A necessary condition for this scheme is that the phase of the signal is stable during the pulse, so that information about the behaviour of the TES does not end up in the Q channel. As this needs to be confirmed for the baseline X-IFU detector, we take for now a conservative approach and leave this factor in.

3.4.1 SQUID + LNA

The behaviour of a SQUID is closely coupled to the properties of the low-noise amplifier with which it is read-out, so we treat the SQUID-LNA system as one, under the assumption that the LNA is well matched to the SQUID and does not add noise. Under baseband feedback, the flux from the carriers on the input coil are fully compensated by the remodulated carriers on the feedback coil, unless there is a signal in one of the pixels. Since only this signal then creates an excursion from the flux setpoint, the dynamic range calculation does not need to include additional margin for the creation of carriers.

In a BBFB system with multiple carriers on a regular grid the gain-bandwidth product (GBW) is limited by the carrier separation Δf to $GBW = \Delta f /2\pi$ [25]. Taking a Δf = 100 kHz, this implies a GBW of ~16 kHz. A minimal measure of the gain by which the pulse excursion from the SQUID setpoint is suppressed by the BBFB is to consider the loopgain at the edge of the information bandwidth B of the pulse, equal to 16 kHz / 1.5 kHz ≅ 10. Current state-of-the-art SQUIDs have a demonstrated noise level of ~0.18 $\mu\Phi_0$/√Hz, which includes the contribution from the LNA as well [5]. Taking these for the moment as a given, the dynamic range requirement provides a maximum rms flux excursion, which will be suppressed by the BBFB loopgain by a factor $1+G \geq 11$. The required SQUID-LNA dynamic range, expressed in units of flux, becomes:

$$DR_\Phi = \frac{\Phi_{pp}}{\phi_n} = 2\sqrt{2}\,\frac{1}{1+G}\,\frac{\Phi_{peak}}{\phi_n} = \frac{8\sqrt{\ln 2}}{(1+G)\sqrt{\tau}}\,\frac{E}{\Delta E} .$$

Using τ = 200 μs, E = 7 keV and ΔE = 0.25 eV cf. the requirements in Section 3.3, we find $DR_\Phi = 1.2\ 10^6$ √Hz, which corresponds, for ϕ_n = 0.18 $\mu\Phi_0$/√Hz to a maximum flux excursion of ~0.2 $\Phi_{0,pp}$, which corresponds to the linearized range of more advanced SQUID amplifiers [39], and agrees with earlier estimates for similar readout systems [6]. In practice, this excursion will be even less due to the finite risetime of the pulses.

3.4.2 DACs and ADC

Both the AC bias and the feedback DACs (see Fig. 2) have to generate a comb of carriers with sufficient dynamic range to allow the modulation by a 12 keV photon, and the high-resolution modulation by a 7 keV photon of each carrier. For the carriers generated by the DACs three additional factors increase the dynamic range requirement:

- For $E < E_{sat,}$ a factor E_{sat}/E, to account for the fact that the modulation depth is maximal only for energy E_{sat} for which the resistance of the detector reaches R_N.
- Even for $E = E_{sat,}$ the modulation depth is limited by the fact that there is still a current $I_{\min} = V_{bias}/R_N$ running, reducing the maximum current change to $\Delta I = V_{bias}/R_0 - V_{bias}/R_N = V_{bias}/R_0\,(1-r)$, with $r = R_0/R_N$. To account for this, the bias power has to be increased by this same factor, where we assume that modulation depth scales linearly with E all the way up to $E_{sat.}$
- A factor $3.5\sqrt{N_{carr}} \cong 22$ for the fact that a superposition of N_{carr} sinusoidal carriers has to be generated, that does not saturate the DAC output. The crest factor (defined as the ratio of the peak amplitude to the rms of a waveform) of 3.5 here is a conservative estimate: with a slightly more dedicated approach, lower values are easily realisable [34].

Hence the dynamic range requirement on the DACs becomes:

$$DR_V = \frac{V_{pp}}{v_n} = 2\sqrt{2}\,\frac{E_{sat}}{E}\,\frac{3.5N_{carr}^{1/2}}{(1-r)}\,\frac{V_{peak}}{v_n} = 2\sqrt{2}\,\frac{3.5N_{carr}^{1/2}}{(1-r)}\,\frac{\sqrt{4\ln 4}}{\sqrt{\tau}}\,\frac{E_{sat}}{\Delta E} = 3.5N_{carr}^{1/2}\,\frac{2\sqrt{2}P_{bias}}{p_{NEP}},$$

where $P_{bias} = E_{sat}/\tau\,/\,(1-r)$ is the bias power, and $p_{NEP} = \Delta E\,/\,(4\ln 4\,\tau)^{1/2}$ is the noise-equivalent power delivering a ΔE contribution to the energy resolution of a pulse with decay time τ. Using $\tau = 200$ μs, $N_{carr} = 40$, $E_{sat} = 12$ keV and $\Delta E = 0.5$ eV (cf. Section 3.3), we find $P_{bias} \cong 12$ pW and $p_{NEP} \cong 2.6$ aW/√Hz, hence $DR_V \cong 1.3\ 10^7$ √Hz per carrier and ~$3\ 10^8$ √Hz in total. The assumption of a single exponential pulse is a worst case from the perspective of DAC DR: a positive risetime will decrease the V_{peak} and thus the required V_{pp}: e.g. a risetime of 25 μs reduces V_{peak} by ~40% and brings P_{bias} to ~7 pW.

The dynamic range that a DAC can deliver, if Δ is the minimal voltage step, N is the effective number of bits, and f_s the sampling frequency, is given by:

$$DR_{DAC} = \frac{V_{pp}}{v_n} = 2^N\Delta \Big/ \frac{\Delta}{\sqrt{12}}\sqrt{\frac{2}{f_s}} = 2^N\sqrt{6f_s}\ .$$

Equating the two expressions for DR and taking $f_s = 20$ MHz [29] results in a requirement of $N \cong 14.7$ effective bits, leaving slightly over one bit of margin above quantization noise. It is also clear that a choice for a smaller contribution to the integrated energy resolution, by demanding that $\Delta E = 0.25$, would lead to an unreasonable requirement. A number of assumptions underlie the above figure:

- All effects due to non-linearity, $1/f$ noise and spurs, as well as noise from the reconstruction filters and series impedances in the bias and feedback lines fall inside the 1 bit of headroom over the full frequency range.
- No margin is taken into account for non-uniformities in the detector set points, the possibility to bias the detectors at a higher set-point resistance, the reduction of the DAC output and the transfer of the bias and feedback circuits towards higher frequencies, etc.

A more detailed assessment of the digital electronics and potential DAC flight candidates has to establish whether 1 bit is indeed all the margin that is possible. For instance, if it were possible to run the DACs at 80 MHz we can create an extra bit of margin.

It is customary in digital electronics to describe the $DR_{\rm DAC}$ as a dB signal-to-noise ratio per unit bandwidth using the expression $SNR_{\rm DAC} = 6.02N + 1.76 + 10\ ^{10}\log ½f_s$, which has to be equated to $SNR_V = 20\ ^{10}\log\,(DR_{V,\rm tot}\,/\,\sqrt{8}) \cong 160$ dB, where the factor $1/\sqrt{8}$ converts peak-to-peak into rms voltages.

The requirements for the ADC are much less tight for two reasons:

- In a baseband feedback system, the carriers are cancelled in the SQUID, unless there is a signal on one of the pixels, resulting in an error signal towards the ADC. Except in cases of heavy pile-up, the ADC typically sees only one pulse at a time. This means that the factor $3.5\sqrt{N_{carr}}$ does not apply for the ADC DR requirement.
- The error signal is suppressed by a factor $(1+G)$.

As a consequence the DR requirement for the ADC is equal to that of the SQUID + LNA combination, which requires only ~7 effective bits for a ADC sampling frequency of 20 MHz, or an $SNR_{\rm ADC} \cong 113$ dB per unit wavelength.

3.5 Crosstalk requirements

Crosstalk is defined as a measurable current change at one frequency ω_i which is the result of a change in resistance in a TES at another frequency ω_j. A quantitive definition is the ratio of the absorbed energy inferred on ω_j to the actual energy deposited in pixel *i*. From this definition follows a minimal requirement for the acceptable level of crosstalk: for each pulse that goes undetected because it falls below the trigger level, the measured apparent energy induced on another frequency must be lower than 0.25 eV. For a maximum trigger level of 200 eV, this would imply a maximum crosstalk level of 0.13%. In practice one would like to set trigger levels as low as possible, as signals below 200 eV (f.i. secondary emission from cosmic ray impacts) should not go undetected. It is also undesirable when pulses with a large energy set off triggers for other pixels in the readout chain.
Crosstalk at the level of 0.13% implies that the minimum trigger level should be at the level of 15 eV to avoid triggering in neighbour pixels by crosstalk from 12 keV photons (which are already pretty rare due to the diminished throughput of the optics and the filters at these energies, and the properties of the X-ray sky). This appears to be a sufficiently low trigger level, although a detailed assessment of the background level in the energy range 0.2 - 15 eV is required for confirmation [35].
Crosstalk at this level requires cross-channel correction for all detected pulses in the event processing software. As the crosstalk mechanisms so far identified are highly predictable, corrections can be calibrated and applied automatically.

There are (at least) four mechanisms which may play a significant role [13][26][36]-[38]:

- Thermal crosstalk on the detector array: heat input on one pixel is able to travel across the array and heat up another pixel. Such crosstalk has been measured in the past for devices such as shown in Fig. 1, and found to be smaller than $4 - 5\ 10^{-4}$. As new detector arrays are still in production, there is no update on this issue.
- Carrier leakage: crosstalk due to the finite bandwidth of the LC filters. A bias voltage applied at a frequency ω_j generates a current in the TES at frequency ω_i, which can get modulated when the resistance of TES *i* changes.
- Common impedance: when the primary circuits of TESs share a common component, such as the input coil of the SQUID, or have coupled coils in their respective LC filters, a current in circuit *i* creates a voltage drop across the common impedance and excites a current in circuit *j*, which then heats up TES *j*.
- SQUID non-linearity, which creates cross products of carriers, in particular higher harmonics of each carrier, which may appear as signals inside the information band of carriers at higher frequencies.

3.5.1 Carrier leakage

If TES *i* undergoes a change in resistance $R_i \rightarrow R_i + \delta R$, it modulates currents of all frequencies ω_j running through it. For exponential pulses in a linear readout system, the measured energy $E \propto \delta I$. If $Z_i(s) = sL_i + 1/sC_i + R_i$ with $s = j\omega$, is the impedance of a primary *LCR* circuit (i.e TES + LC filter), then:

$$\frac{\delta I(\omega_j)}{\delta I(\omega_i)} = \frac{\dfrac{V_b}{Z_i(s_j)+\delta R} - \dfrac{V_b}{Z_i(s_j)}}{\dfrac{V_b}{R_i+\delta R} - \dfrac{V_b}{R_i}} \approx \left(\frac{R_i}{2(\omega_i - \omega_j)L_i} \right)^2 ,$$

3.5.2 Common impedance

Consider a common impedance Z_c in series with all the parallel primary *LCR* circuits (see Fig. 2). An applied bias voltage V_b will be divided across the parallel circuits and Z_c. The voltage across the TES circuits is then given by

$$V_{TES}(\omega) = \frac{Z_{par}(\omega)}{Z_{par}(\omega) + Z_c(\omega)} V_b(\omega) \quad \text{where} \quad Z_{par}(\omega) = \left(\sum_i Z_i(\omega)^{-1} \right)^{-1}$$

The current through TES *j* at frequency ω_i is then $I_j(\omega_i) = V_{TES}(\omega_i) / Z_j(\omega_i)$ and the power dissipated in TES *j* as a result of this current is $P_j(\omega_i) = I_j(\omega_i)^2 R_i$. Next to carrier leakage, similar to the previous section, there is another crosstalk mechanism due to the fact that a current $\delta I_i(\omega_i)$ through common impedance Z_c will create a voltage drop $\delta V_c(\omega_i) = Z_c(\omega_i)\ \delta I_i(\omega_i)$ [26]. This then creates a current in TES *j*: $\delta I_j(\omega_i) = -\delta V_c(\omega_i) / Z_j(\omega_i)$, which will dissipate power

$\delta P_j = 2I_j(\omega_i)\,\delta I_j(\omega_i)R_j$, which will create a current change at frequency ω_j: $\delta I_j(\omega_j) = \delta P_j / V_{TES}(\omega_j)$. The resulting crosstalk signal can be approximated as $\delta I(\omega_j)/\delta I(\omega_i) \cong (L_c\omega_i/2L_i\Delta\omega)^2$ [38].

If the inductance of the SQUID input coil is the main common impedance, and the input and feedback coils are coupled, the BBFB loop will partially suppress this form of crosstalk. Assuming uncoupled input and feedback coils, and a resistance change from set point (0.2 R_N) to normal, Table 4 lists the crosstalk values between nearest and second neighbours in frequency. This implies that crosstalk correction for a pulse is mainly required between nearby frequencies, which alleviates the computational burden on the event processing considerably. The requirements on L_F and L_c are not absolute, although Table 4 suggests ballpark ranges. A L_F = 1 μH would allow stable ETF voltage biasing of the TESs at a 0.2 R_N setpoint without impedance transformation across the coupling coils, while L_F = 2 μH provides the smallest area LC filter chips and a more feasible budget for the common impedance. LC filters based on larger L_F would be part of a design trade-off. A common inductance L_c > 3 nH, even in combination with L_F = 2 μH, might still be acceptable, but will narrow the range of trigger thresholds.

	L_F = 1 μH, L_c = 1 nH n_p:n_s = 1:1			L_F = 2 μH, L_c = 2 nH n_p:n_s = 1.4:1			L_F = 3 μH, L_c = 4 nH n_p: n_s = 1.7:1		
Carrier frequency	1 MHz	3 MHz	5 MHz	1 MHz	3 MHz	5 MHz	1 MHz	3 MHz	5 MHz
Carrier leakage	0.10%	0.10%	0.10%	0.097%	0.097%	0.097%	0.094%	0.094%	0.094%
Common impedance	0.003%	0.023%	0.063%	0.0033%	0.036%	0.11%	0.004%	0.040%	0.11%
Combined Δf=100 kHz	0.10%	0.10%	0.12%	0.097%	0.10%	0.12%	0.094%	0.11%	0.15%
Combined Δf=200 kHz	0.025%	0.026%	0.030%	0.024%	0.025%	0.029%	0.024%	0.026%	0.036%

Table 4. Crosstalk levels for various combinations of filter and common inductance, carrier frequency and carrier separation. Included are turn ratios for the coupling coils, which are applied to ensure ETF stability.

3.5.3 Linearity of the amplifier chain

The requirement on the linearity of the SQUID response has its origin in the crosstalk requirements. Ideally, the total harmonic distortion (THD) should be so low that a pulse loses less than 0.25 eV per higher harmonic component, so that if it happens that a higher harmonic product coincides with the information band around another carrier, it creates an error within the allowed noise apportionment. As a practical measure, a total loss of 0.2% of signals within an input range of 0.5 $\Phi_{0,pp}$ has been set as a requirement [39][40]. The main difference with crosstalk is the non-linear character of the harmonic products, which makes correction in the event processor practically impossible. The open-loop output of the SQUID is given by [6][39]:

$$V_{out}(f) = k_1\Phi_{in}(f) + k_2\Phi_{in}^2(f) + k_3\Phi_{in}^3(f) + \text{ higher order terms.}$$

In this expression k_i are the coefficients, and $\Phi_{in} = L_{in}\,I_{sum} / \Phi_0$ the flux in the SQUID due to the summed currents on the input coil. The first term is the linear response of the SQUID, while the THD consists mainly of the second and third order terms [40]. If we normalize to k_1=1, an actual (PTB) SQUID shows k_1=0.4 and k_3=13. When feedback is applied with a loopgain $\mathscr{L}(f)$, the input flux Φ_{in} is reduced by the counter flux from the feedback coil to $\Phi_{in} / [1+\mathscr{L}(f)]$, while the non-linear terms receive an additional suppression, as they can be regarded as gain errors in the forward path of the feedback loop:

$$V_{out} = k_1\left(\frac{\Phi_{in}(f)}{[1+\mathscr{L}(f)]}\right) + \frac{1}{[1+\mathscr{L}(f)]}\left[k_2\left(\frac{\Phi_{in}(f)}{[1+\mathscr{L}(f)]}\right)^2 + k_3\left(\frac{\Phi_{in}(f)}{[1+\mathscr{L}(f)]}\right)^3 + \text{higher order terms}\right].$$

Both VTT [39] and PTB [40] have demonstrated SQUIDs with externally applied feedback for linearization, and obtained 0.2% THD figures for input ranges between 0.25 to 0.7 $\Phi_{0,pp}$, with loopgains of the order of 16 and 20, respectively. Both groups are also working on the implementation of local linearization schemes, in combination with two-stage designs, which would aid the loopgain provided by BBFB with an additional gain of 4 - 5 [41]. More detailed

analysis is required to confirm that this is sufficient suppression to make the effects of individual harmonics practically negligible.

3.6 Summary of read-out requirements

Table 5 summarizes the main requirements on the read-out system:

Parameter	Requirement	Comments
Frequency range	1 - 5 MHz	Goal is an upper limit of 6 MHz to create some margin on the carrier separation
Number of carriers	40	Number of pixels / maximum number of channels
Carrier separation	100 kHz	Frequency range / number of carriers
Q_{LC}	> 3000 f [MHz]	Routinely demonstrated
Dynamic range of SQUID + LNA	> 1.2 10^6 √Hz	Corresponds with flux excursions ≤ 0.3 $\Phi_{0,pp}$
Dynamic range of ADC	7 bits	Effective number of bits corresponding to DR of SQUID + LNA combination
SNR ADC	113 dB	Per unit frequency
Dynamic range of DACs	> 1.3 10^7 √Hz	Per carrier
	> 3 10^8 √Hz	For a comb of 40 carriers
	15 bits	Effective number of bits in the DAC, in case quantization noise dominates and 20 MHz sampling
SNR DACs	160 dB	Per unit frequency
Crosstalk	< 0.13%	Restricts the trigger level to 15 - 200 eV. Requires correction in the event processing.
SQUID linearity (THD)	< 0.13%	TBC

Table 5. Summary of requirements on the readout system.

4. CONCLUSIONS

In this paper we made a start with the definition of the main requirements for the X-IFU detector and readout system, derived from a set of top-level instrument requirements which follow from the Athena science case. We focussed here on top-level dynamic range and crosstalk requirements. In the requirements of the readout system derived so far we did not encounter show-stoppers, although the dynamic range requirement on the AC-bias and feedback DACs leaves currently little margin. More margin may be created by running the DACs at higher frequencies or require the development of more advanced DACs, but may also be created with more advanced event processing algorithms, which allow the required count rate capability for longer pulse decay times. This work is far from finished: more details in the end-to-end processing of photon signals need to be assessed, and more iterations are required as the detectors and the cooler system will take shape the coming years.

REFERENCES

[1] Nandra, K., Barret, D., Barcons, X., et al. 2013, "The Hot and Energetic Universe: A White Paper presenting the science theme motivating the Athena mission", arXiv 1306.2307 (2013)

[2] Nandra, K., Barret, D., Barcons, X., et al. 2014, "Athena: The Advanced Telescope for High-Energy Astrophysics", Mission proposal submitted to ESA, http://www.the-athena-x-ray-observatory.eu/ (2014)

[3] Ravera, L., Barret, D., den Herder, J.W., et al., "The X-ray Integral Field Unit (X-IFU) for Athena", these proceedings 9144-92 and http://www.the-athena-x-ray-observatory.eu/ (2014)

[4] den Herder, J.W., Kelley, R.L., Mitsuda, K., et al. "The X-ray Microcalorimeter Spectrometer onboard of IXO", Proc. SPIE 7732, 77321H (2010)

[5] Gottardi, L., et al. "Development of TES-based detectors array for the X-ray Integral Field Unit (X-IFU) on the future X-Ray Observatory ATHENA", these proceedings, 9144-93 (2014)

[6] de Korte, P., et al., "EURECA – A European-Japanese micro-calorimeter array", J. Low Temp. Phys. 151, pp. 733-739 (2008)

[7] H.J. van Weers, J.-W. den Herder, B.D. Jackson, P.P. Kooijman, " TES-detector based focal plane assembly key-technology developments for ATHENA and SAFARI", these proceedings, paper 9144-225 (2014)
[8] Smith S., et al., "Implications of weak-link behavior on the performance of Mo/Au bilayer transition-edge sensors", J. Appl. Phys. 114, 074513 (2013)
[9] Irwin, K., "Thermodynamics of nonlinear bolometers near equilibrium", NIM A 559, 718-720 (2006)
[10] J.N. Ullom, W.B. Doriese, G.C. Hilton, J.A. Beall, S. Deiker, W.D. Duncan, L. Ferreira, K.D. Irwin, C.D. Reintsema and L.R. Vale, "Characterization and reduction of unexplained noise in superconducting transition edge sensors", Appl. Phys. Lett. 84, 4206-4208 (2004).
[11] Takei, Y., Gottardi, L., et al. "Characterization of a high-performance Ti/Au TES microcalorimeter with a central Cu absorber", J. Low Temp. Phys. 151, 161-166 (2008)
[12] Ullom, J., et al., "Optimized transition-edge x-ray microcalorimeter with 2.4 eV energy resolution at 5.9 keV", Appl. Phys. Lett. 87, 194103 (2005)
[13] Dirks, B.P.F., Popescu, M., Bruijn, M., Gottardi, L., Hoevers, H.F.C., de Korte, P.A.J., van der Kuur, J., Ridder, M. and Takei, Y., "TiAu-based micro-calorimeters for space applications", Nucl. Instum. Meth. A 610, 83-86 (2009).
[14] Gottardi, L., Takei, Y., et al. "Characterisation of a TES-based X-ray microcalorimeter in the energy range from 150 to 1800 eV using an Adiabatic Demagnetisation Refrigerator", J. Low Temp. Phys. 151, 106-111 (2008)
[15] K.D. Irwin and G.C. Hilton, "Transition-Edge Sensors" in Cryogenic Particle Detection, edited by C. Enss, Springer-Verlag, Berlin Heidelberg, 2005, vol. 99 of Topics in Applied Physics, pp. 63–149.
[16] Kilbourne, C. et al., "Multiplexed read-out of uniform arrays of TES X-ray microcalorimeters suitable for Constellation-X ", Proc SPIE 7011, 701114 (2008)
[17] Bandler, S., Adams, J., Busch, S., et al. " Development of large arrays of small pixels for x-ray astrophysics", these proceedings, 9144-34 (2014)
[18] Gottardi, L., et al. "AC read-out circuits for single pixel characterization of TES microcalorimeters and bolometers", IEEE Trans. Supercond. 21(3), 272-275 (2010)
[19] Gottardi, L., et al. "Study of the Dependency on Magnetic Field and Bias Voltage of an AC-Biased TES Microcalorimeter", J. Low Temp. Phys. 167, 214-219 (2012)
[20] Kirsch, M.G., "Crab: the standard candle with all (modern) x-ray satelites", Proc. SPIE 5898, 589803 (2005)
[21] Wilms, J., Barret, D., Beuchert, T., Brand, T., den Herder, J.-W. et al. "Athena end-to-end simulations," these proceedings, 9144-231 (2014)
[22] Doriese, W.B., et al. "Optimal filtering, record length, and count rate in transition-edge-sensor microcalorimeters", LTD-13 AIP Conf. Proc. 1185, 450-453 (2009)
[23] M. Kiviranta, H. Seppä, J. van der Kuur, and P. de Korte, "SQUID-based Readout Schemes for Microcalorimeter Arrays", AIP Conf. Proc. 605, 295 – 300 (2002)
[24] J. Yoon, et al., "Single SQUID Multiplexer or Arrays of Voltage-biased Superconducting Bolometers", AIP Conf. Proc. 605, 305 – 308 (2002)
[25] R. den Hartog et al., "Baseband Feedback for Frequency-Domain-Multiplexed Readout of TES X-ray Detectors", LTD-13 AIP Conf. Proc. 1185, 261-264 (2009)
[26] M. Dobbs et al., "Frequency multiplexed superconducting quantum interference device readout of large bolometer arrays for cosmic microwave background measurements", Rev. of Scientific Instruments 83, 073113 (2012)
[27] J. van der Kuur, J. Beyer, M. Bruijn et al. "The SPICA-SAFARI TES Bolometer Readout: Developments Towards a Flight System", J. Low Temp. Phys. 167, 561-567 (2012)
[28] B. D. Jackson, P. A. J. de Korte, J. van der Kuur et al. "The SPICA-SAFARI Detector System: TES Detector Arrays with Frequency Division Multiplexed SQUID Readout", IEEE Trans. Terahertz Sc. Techn. 2, 12-21 (2012)
[29] Ravera, L., et al. "The DRE, the digital readout electronics for Athena X-IFU", these proceedings, 9144-227 (2014)
[30] M.P. Bruijn et al., "High-Q LC Filters for FDM Readout of Cryogenic Sensor Arrays", J. Low Temp. Phys. 167, 695-700 (2012)
[31] J. van der Kuur, L. Gottardi, M.P. Borderias et al. "Small-Signal Behaviour of a TES under AC Bias", IEEE Trans. Appl. Supercond. 21, 281-284 (2011).
[32] Sadleir, J., Smith, S., Bandler, S.R., Chervenak, J.A., Clem, J.R., "Longitudinal Proximity Effects in Superconducting Transition-Edge Sensors", PRL 104, 0470003 (2010)
[33] Gottardi, L., Akamatsu, H., Bruijn, M. et al., "Weak-Link Phenomena in AC-Biased Transition Edge Sensors", J. Low Temp. Phys., in press (2014)
[34] M. Lindeman et al., "Carrier Phase Optimization for Frequency Division Multiplexing of Low Temperature Detectors", J. Low Temp. Phys. 167, 701-706 (2012)

[35] Lotti, S., Macculi, C., et al., "Background simulations for the ATHENA X-IFU instrument: impact on design and scientific performances", these proceedings, 9144-95 (2014)
[36] de Korte, P., et al., "EURECA – A European-Japanese micro-calorimeter array", Proc. SPIE 6266, 62661Z (2006)
[37] den Hartog, R., et al. "Frequency Domain Multiplexed Readout of TES Detector Arrays with Baseband Feedback", IEEE Trans. Appl. Supercond., Vol 21, 289 (2011)
[38] J. van der Kuur, P.A.J de Korte, P. de Groene, N.H.R. Baars, M.P. Lubbers, M. Kiviranta, "Implementation of frequency domain multiplexing in imaging arrays of microcalorimeters", Nucl. Instr. Meth. A 520, 551-554 (2004)
[39] Kiviranta, M., "SQUID linearization by current-sampling feedback", Supercond. Sci. Technol. 21**,** 045009 (2008)
[40] D. Drung, J. Beyer et al., "Novel SQUID Current Sensors With High Linearity at High Frequencies", IEEE Trans. Appl. Supercond. 19, vol. 3, 772-777 (2009)
[41] Kiviranta, M., and Grönberg, L., "Progress Towards Large Locally Linearized SQUID Arrays", LTD-13 AIP Conf. Proc. 1185, 526-529 (2009)